https://doi.org/10.48047/AFJBS.6.14.2024.9383-9403

African Journal of Biological Sciences

Journal homepage: http://www.afjbs.com

Research Paper Open Access

STRUCTURAL AND COMPUTATIONAL ANALYSIS OF A FLAVONOID FROM *ELAEOCARPUS SERRATUS* FOR POTENTIAL ANTICANCER ACTIVITY

FASEELA V A[1], P. MAHESHWARI*[2],

[1]Research scholar, School of Pharmaceutical Sciences, Department of Pharmacy Practice, School of Pharmaceutical Sciences, Vels Institute of Science, Technology and Advanced Studies (VISTAS) Pallavaram, Chennai, India

[*2] Associate Professor, Department of Pharmacy Practice, School of Pharmaceutical Sciences, Vels Institute of Science, Technology and Advanced Studies (VISTAS) Pallavaram, Chennai, India

Corresponding Author: Dr P Maheshwari

Associate Professor,Department of Pharmacy Practice, School of Pharmaceutical Sciences, Vels Institute of Sciences, Technology and Advanced Studies (VISTAS), Pallavaram, Chennai-600117, India E-mail:mahe.mpharm@gmail.com Mob :+919677192659

Volume 6, Issue 14, Aug 2024

Received: 15 June 2024

Accepted: 25 July 2024

Published: 15 Aug 2024

doi: 10.48047/AFJBS.6.14.2024.9383-9403

Abstract

Background: *Elaeocarpus serratus*, known for its diverse medicinal properties, has been investigated for its potential as an anticancer agent. This study focused on isolating bioactive compounds and evaluating their binding affinities and stabilities using *in silico* methods.

Methods: The ethyl acetate-soluble portion of *the E. serratus* leaf extract was subjected to column chromatography, yielding a single compound. The structure was elucidated by IR, ^{1}H NMR, ^{13}C NMR, and LC-MS. *In silico* docking studies were performed using AutoDock, followed by all-atom molecular dynamics (MD) simulations to examine the protein-ligand interactions. The parameters analyzed included Root Mean Square Deviation (RMSD), Root Mean Square Fluctuation (RMSF), Radius of Gyration (Rg), solvent-accessible surface area (SASA), and hydrogen bond formation. The binding affinities were calculated using the MM-PBSA method.

The isolated compound was identified as 3,8-dihydroxy-6-(hydroxymethyl)-2-(3-methoxy-5-methylphenyl)-4H-chromen-4-one. Docking results revealed a strong binding affinity for the drug compound (DRG) with a score of -8.4, compared to the standard inhibitor androstenedione (STD) with a score of -7.6. MD simulations indicated stable protein-ligand interactions, with average RMSD values of 0.26 ± 0.03 nm (APO), 0.36 ± 0.04 nm (ASD), and 0.33 ± 0.05 nm (DRG). The RMSF and Rg values suggest similar flexibility and compactness across complexes. MM-PBSA analysis confirmed strong binding affinities, with DRG showing slightly higher van der Waals and electrostatic interactions.

Conclusion: The flavonoid isolated from *E. serratus* demonstrated strong binding affinity and stability in protein-ligand interactions, indicating its potential as a therapeutic agent for breast cancer treatment. Further in vivo studies are warranted to explore their efficacy.

Keywords: Elaeocarpus serratus, Flavonoid isolation, Molecular docking, Protein-ligand interactions

Introduction

Elaeocarpus serratus, or Ceylon olive, is a tropical tree up to 20 m tall with distinctive buttresses and a mottled brown-grey bark.[1] The young

parts are covered with dense, velvet-like hairs. Leaves are simple, alternate, and leathery, with elliptical shapes and saw-toothed margins. White bisexual flowers grow in leaf axil racemes with five velvet-hairy sepals and five laciniate petals. This fruit is a green drupe with a single seed.[2-4] Native to Sri Lanka and southern India and extending to Assam and Bangladesh in the northern Indian subcontinent, *E. serratus* has a unique distribution pattern that encompasses both tropical and subtropical regions.[5-8]

In the past, *E. serratus* leaves were commonly used to treat rheumatism and as an antidote, whereas the fruits were known to alleviate diarrhea and dysentery.[9] A wide range of bioactive compounds, such as alkaloids, flavonoids, tannins, and triterpenes, support the medicinal value of plants. The compounds in question possess various beneficial properties, including antioxidant, antidiabetic, antimicrobial, analgesic, anti-inflammatory, and antihypertensive effects, indicating the therapeutic potential of *E. serratus*. Recent pharmacological investigations have uncovered the antibacterial activity of *E. serratus* leaves against a range of pathogens, as well as their potential as antitumor and pesticidal agents. It is important to note that *E. serratus* contains flavonol glycosides such as myricitrin and tamarixetin 3-O-α-L-rhamnopyranoside. In addition, nanoparticles obtained from various tree parts have shown antimicrobial properties against various strains.[10-14]

Breast cancer continues to be a significant contributor to cancer-related deaths globally, demonstrating the urgency for the development of innovative and efficient treatments with minimal adverse effects. Throughout history, natural products have been crucial in the exposure to effective anticancer drugs. Examples, such as paclitaxel and vinblastine, demonstrate immense therapeutic possibilities that can be found in plant-derived compounds. [15] Flavonoids found in *E. serratus* are well-known for their antioxidant and anti-inflammatory properties, making them important for cancer prevention and treatment. These compounds have demonstrated the ability to trigger programmed cell death, hinder cell growth, and regulate cancer-associated signaling pathways. [16]

Early research on *E. serratus* demonstrated its antibacterial, antioxidant, and anticancer properties, indicating that it may be a promising candidate for novel cancer treatments. The existence of bioactive flavonoids, such as tamarixetin and myricitrin, emphasizes the need for further research into the possible anticancer effects of *E. serratus* on breast cancer. Therefore, investigating the anticancer efficacy of this plant is crucial for developing new cancer therapies and expanding our knowledge of plant-based medicinal agents.

MATERIALS AND METHODS

Sample Collection

Fresh leaves of *E serratus* were collected in January from Sugandhagiri, Wayanad district, Kerala. The scientific authenticity of the specimens was verified by Dr. Sreekumar V.B, Senior Scientist at the Forest Botany Department, Kerala Forest Research Institute (KFRI), Peechi, Thrissur, Kerala. The specimens were accessioned to the KFRI herbarium under the accession number 1835. The collected plant specimens were thoroughly cleaned with running freshwater to remove any adhering dirt and debris. Subsequently, the leaves were air-dried in the shade for approximately two weeks. Once dried, they were ground into a fine powder and stored in sealed bags for further research.

Extraction

Air-dried, powdered leaves (100 g) of the plant were subjected to successive solvent extraction using solvents of increasing polarity, including chloroform, ethyl acetate, ethanol, and water. Initially, the powdered leaves were defatted using petroleum ether. Following defatting, the samples were placed in an orbital shaker for 48 hours. The supernatant was then collected and filtered through Whatman No. 1 filter paper. After extraction, the crude extract solution was concentrated using a rotary evaporator, yielding 5 g of the residue. The crude extract was washed with petroleum ether to remove nonpolar impurities. [17-18]

The percentage yield of the extracts was calculated as follows:

$$\text{Percentage yield} = (W_2/ W_1) \times 100$$

Where,

W_1 =Weight of the dried plant material taken

W_2 =Weight of the extract obtained

Isolation of phytochemicals using column chromatography

The ethyl acetate-soluble portion of the crude extract from *E. serratus* was subjected to column chromatography using a silica gel column that served as the stationary phase. The extract was loaded onto the top of the silica gel column, and elution was performed using a solvent mixture of 30% ethyl acetate and 70% petroleum ether. This solvent system was chosen to balance the polar and nonpolar environments, facilitating the effective separation of phytochemical constituents.

The column was eluted under gravity, and the fractions were systematically collected. A gradient elution approach was adopted to separate compounds with varying polarities precisely. Each collected fraction was monitored by thin-layer chromatography (TLC). The TLC plates were developed and visualized to determine the retention factor (Rf) values of the eluted compounds. The fractions exhibiting similar Rf values were mixed, indicating the presence of similar compounds. For structural elucidation, the isolated compound was subjected to extensive spectroscopic analysis using FT-IR, 1H NMR, and 13C NMR spectroscopy to elucidate the structure and LCMS to confirm the identity and purity of the isolated compound. [19-20]

***In-silico* docking studies**

Molecular docking studies were conducted using AMDock v.1.5.2, using the AutoDock engine for robust docking. AMDock integrates essential tools, such as Open Babel, PDB2PQR, and PyMol, for comprehensive structural analysis (Valdés-Tresanco et al., 2020). Docking results were evaluated based

on the binding affinity (kcal/mol), estimated Ki (μM), and ligand efficiency. Ki values were calculated using AutoDock Vina with the equation exp(ΔG/RT), where R is the universal gas constant (1.985×10^{-3} kcal mol^{-1} K^{-1}), and T is the temperature (298.15 K). The compound exhibiting the most negative binding affinity and lowest Ki value was selected as the optimal ligand. [21-22]

Molecular Dynamics

The crystal structure of human placental aromatase cytochrome P450 in complex with androstenedione (PDB ID: 3EQM) was used for molecular dynamics simulations. The top ligands identified from the docking analysis, including the standard androstenedione (ASD) and drug (DRG), were selected. Ligand topology was obtained using the ATB server. The pdb2gmx module of GROMACS was used to add hydrogen to the heavy atoms. The prepared systems were first vacuum-minimized for 1500 steps using the steepest descent algorithm. Subsequently, the structures were solvated in a cubic periodic box with an SPCE water model and maintained at a salt concentration of 0.15 M by adding Na and Cl counter ions, following procedures from a previous study (PMID: 31514687).

Each structure from the NPT equilibration phase was subjected to a final production run in the NPT ensemble for a simulation time of 100 ns. The simulation trajectories were analyzed using various GROMACS tools to assess the protein root mean square deviation (RMSD), root mean square fluctuation (RMSF), radius of gyration (RG), solvent-accessible surface area (SASA), and hydrogen bonding (H-bond). The Molecular Mechanics Poisson-Boltzmann Surface Area (MM-PBSA) approach was employed to determine the binding free energy of the inhibitor with the protein over the simulation period. The GROMACS utility g_mmpbsa was used to estimate the binding free energy (Kumari et al., 2014), with calculations performed for the last 50 ns of the simulation at intervals of 1000 frames for accurate results. [23-25]

RESULTS

Isolation

One compound was isolated from the *E. serratus* leaf extract, which showed a distinct band with an Rf value of 0.3. The fractions corresponding to this Rf value were combined and concentrated using a rotary evaporator to remove the solvent. The concentrated fractions were thoroughly dried, yielding a final product weighing 10 mg (Figure 1&2).

Spectroscopic analysis of the compound isolated from *E. serratus* provided the following data:

IR Spectroscopy (υ_{max}, cm^{-1}, KBr): A strong, broad peak at 3258 cm^{-1} indicates the presence of hydroxyl groups (OH), and a sharp peak at 1827 cm^{-1} corresponds to carbonyl groups (C=O) (Figure 3).

The ^{1}H NMR (400 MHz, DMSO) spectrum of the flavonoid revealed several distinct peaks, corresponding to various proton environments within the molecule. A singlet at δ 1.25 indicates the presence of a methyl group ($-CH_3$) with three protons, while another singlet at δ 3.28, integrating for one proton, confirms a methoxy group ($O-CH_3$). A singlet at δ 4.14, representing three protons, indicates a hydroxyl group (–OH). The doublet of doublets at δ 4.49, with two protons and a coupling constant (J) of 2.2 Hz, suggests a methylene group ($-CH_2$) adjacent to another functional group. A singlet at δ 5.64, with one proton, points to another hydroxyl group (-OH). The multiplet between δ 7.23 and 8.18, integrating for five protons, signifies the presence of hydrogen atoms in an aromatic ring, characteristic of the benzene rings in the flavonoid structure. Finally, a singlet at δ 10.6, with one proton, confirmed another hydroxyl group (-OH). These proton signals collectively indicate the presence of methyl, methoxy, methylene, and multiple hydroxyl groups along with aromatic hydrogen atoms, which is consistent with the structure of a flavonoid compound (Figure 4).

The ^{13}C NMR spectrum of the isolated flavonoid reveals peaks indicative of various functional groups. The chemical shift at δ 22.3 corresponds to a methyl group (-CH_3), while the shift at δ 47.6 suggests a carbon adjacent to a methoxy group (-OCH_3). The peak at δ 60.25 is characteristic of the methoxy group. The values between δ 110.87 and 112.12 (7C) and δ 129.34 are typical of aromatic carbon atoms within the benzene rings of the flavonoid structure. The shift at δ 140.64 indicates a carbon atom within an aromatic ring bonded to an oxygen atom, and δ 146.32 is associated with carbon in a conjugated aromatic system, likely attached to a hydroxyl group. Finally, the peaks between δ 159.82 and 160.25 (5C) suggest highly deshielded carbons, such as those in the carbonyl groups (C=O) and conjugated aromatic systems. These shifts collectively confirmed the presence of methyl, methoxy, aromatic, phenolic, and carbonyl functionalities within the flavonoid compound. This analysis confirmed the presence of 18 carbon atoms in the isolated compounds (Figure 5).

LC-MS Analysis: The purity of the isolated compound was 92%, with a retention time (RT) of 1.65 minutes. The calculated molecular weight of the compound $C_{18}H_{16}O_6$ is 328.09 m/z, confirmed by LC-MS showing a [M+1] peak at 329.25 m/z (Figure 6&7). The IUPAC name of the isolated compound is 3,8-dihydroxy-6-(hydroxymethyl)-2-(3-methoxy-5-methylphenyl)-4H-chromen-4-one.

In-silico docking studies

The protein model was subjected to molecular docking using AutoDock, resulting in docking scores that indicate the binding affinities of the compounds. The docking score for the standard inhibitor, androstenedione (STD) was − -7.6, while the docking score for the drug compound (DRG) was -8.4, suggesting a stronger binding affinity for DRG (Table 1). The docking results revealed that the DRG compound exhibited a strong binding affinity with a docking score of -8.4, interacting with key residues such as CYS437, VAL370, and VAL373. In comparison, the standard compound (STD) showed a slightly lower docking score of -7.6 and interacted with a broader range of residues, including

MET364, MET447, PHE430, SER314, PRO429, VAL370, VAL373, and CYS437. These interactions suggest that the DRG has a more specific binding pocket, whereas the STD interacts with multiple sites on the protein.

Molecular Dynamics (MD) Simulations

All-atom molecular dynamics (MD) simulations were performed to examine the structural dynamics of the protein and its interactions with the ligands. This method has significantly advanced computer-aided drug design and discovery by providing detailed atomic-level insights into molecular systems. In this study, MD simulations were conducted to investigate the dynamic changes that occur upon the binding of the target protein to the ligands. Several parameters were calculated for both the protein and protein-ligand complex during the MD simulations, including Root Mean Square Deviation (RMSD) to assess the overall stability of the protein structure over time, Root Mean Square Fluctuation (RMSF) to measure the flexibility of individual residues in the protein, Radius of Gyration (Rg) to evaluate the compactness of the protein structure, Solvent Accessible Surface Area (SASA) to determine the surface area of the protein accessible to solvent molecules, and intermolecular hydrogen bonding to analyze the number and stability of hydrogen bonds between the protein and ligand. These parameters provide a comprehensive understanding of the structural dynamics and interactions within the protein-ligand complex, aiding the evaluation of binding affinity and stability, which are crucial for drug design and development (Figure 8).

Root Mean Square Deviation (RMSD)

Stability of the protein-ligand complexes and their behavior were analyzed by RMSD values (Figure 9). The results indicate that all systems reached equilibrium within 10 ns and remained stable throughout the 100 ns simulation. The RMSD analysis showed that the APO, ASD, and DRG complexes maintained stability, with average RMSD values of 0.26 ± 0.03 nm, 0.36 ± 0.04 nm, and

0.33 ± 0.05 nm, respectively. These findings suggest that the docked complexes did not exhibit significant fluctuations during the simulation, indicating that the protein-ligand interactions were stable and the systems were robust.

Root Mean Square Fluctuation (RMSF)

It helps to measure the fluctuations of each residue and identify flexible regions in a protein during molecular dynamics (MD) simulations. RMSF helps to determine the impact of ligand binding on protein dynamics. Generally, compact protein structures, such as sheets and helices, exhibit lower RMSF values, whereas loosely ordered loop regions show higher RMSF values. The RMSF values were calculated and plotted for each residue in the APO, ASD, and DRG complexes (Figure 10). The average RMSF values for APO, ASD, and DRG were 0.13 ± 0.06 nm, 0.14 ± 0.07 nm, and 0.14 ± 0.06 nm, respectively. These results suggest that the binding of ligands in the ASD and DRG complexes did not significantly alter the overall RMSF distribution compared to the APO complex, indicating that the structural flexibility of the protein was not substantially affected by ligand binding.

Radius of gyration (Rg)

Radius of gyration (Rg) values were computed and plotted over time to assess the dynamic stability and compactness of the APO, ASD, and DRG complexes, the radius of gyration (Rg) values were computed and plotted over time (Figure 11). The average Rg values for APO, ASD, and DRG were 2.26 ± 0.01 nm, 2.25 ± 0.01 nm, and 2.27 ± 0.01 nm, respectively. These results indicated that the Rg values of the APO and ASD complexes were almost identical to those of the DRG complex, suggesting that all three systems maintained similar levels of compactness throughout the simulation. This similarity in Rg values implies that the binding of ligands in the ASD and DRG complexes does not significantly affect the overall compactness and structural integrity of the protein compared with the APO complex.

Solvent accessible surface area (SASA)

SASA values were calculated and plotted for the APO, ASD, and DRG complexes (Figure 12) to evaluate the accessibility of the protein molecule in a solvent environment. The analysis revealed a similar pattern in SASA values across all three complexes. The average SASA values were 217.44 ± 4.3 nm² for APO, 212.49 ± 6.7 nm² for ASD, and 218.69 ± 4.3 nm² for DRG. These results indicate that the SASA values equilibrated well without significant fluctuations throughout the simulation, suggesting that the binding of the DRG ligand does not substantially alter the solvent accessibility of the target protein compared with the APO and ASD complexes. This consistency in SASA values implies that the overall solvent exposure of the protein remained stable, regardless of ligand binding.

Intra and Inter Hydrogen Bond

The formation of intra- and inter-hydrogen bonds is crucial for assessing the stability of protein-alone (APO) and protein-ligand (ASD and DRG complex) interactions. The time-dependent behavior of intra-hydrogen bonds in APO, ASD, and DRG complexes was studied and plotted the results (Figure 13). The average intra-hydrogen bond values were 351.85 ± 9.1 for APO, 356.92 ± 9.92 for ASD, and 358.88 ± 9.5 for DRG. The plot revealed that both the ASD and DRG complexes formed more hydrogen bonds than the APO form of the protein. This increase in hydrogen bonds indicates that the ASD and DRG complexes exhibit greater stability than the APO form, suggesting that ligand binding enhances the overall structural stability of the protein.

The formation of hydrogen bonds plays a crucial role in assessing the stability of protein–ligand interactions. In this study, we investigated the time-dependent behavior of hydrogen bonds in DRG complexes and plotted the results (Figure 14). Our analysis indicated that the docked complex remained stable throughout the simulation, consistently maintaining two to nine hydrogen bonds with

the DRG ligand. This stability suggests that the interactions between the protein and the DRG ligand are robust and contribute to the overall structural integrity of the complex.

MM - PBSA

To determine the binding affinities of APO, ASD, and DRG, we examined their relative binding strengths within the protein using the MM-PBSA method. Table 2 compares the van der Waals energy, electrostatic energy, polar solvation energy, and overall binding energy for APO, ASD, and DRG inhibitors computed over a stable simulation trajectory with residue-level contributions to the interaction energy.

The results show that the ASD complex has a van der Waals energy of -171.255 ± 13.234 kJ/mol, electrostatic energy of -13.363 ± 4.969 kJ/mol, polar solvation energy of 88.872 ± 4.155 kJ/mol, and binding energy of -112.925 ± 10.849 kJ/mol. In comparison, the DRG complex had a van der Waals energy of -186.716 ± 10.310 kJ/mol, an electrostatic energy of -46.321 ± 10.450 kJ/mol, a polar solvation energy of 154.372 ± 10.519 kJ/mol, and a binding energy of -98.144 ± 12.154 kJ/mol. These values indicate that both the ASD and DRG complexes exhibit strong binding affinities, with DRG showing slightly higher van der Waals and electrostatic interactions, whereas ASD has a more favorable overall binding energy.

SUMMARY

One flavonoid was isolated from the ethyl acetate leaf extract of *E. serratus* through silica gel-based column chromatography, and its structure was established with sophisticated analytical support such as FT-IR, ^{1}H NMR, and ^{13}C NMR. The isolated compound, 3,8-dihydroxy-6-(hydroxymethyl)-2-(3-methoxy-5-methylphenyl)-4H-chromen-4-one, was subjected to in silico docking. It is performed using AutoDock analysis revealed that the drug compound (DRG) exhibited a stronger binding affinity (-8.4) than the standard inhibitor androstenedione (STD) (-7.6), interacting specifically with residues such as

CYS437, VAL370, and VAL373. All-atom molecular dynamics (MD) simulations were used to further examine the structural dynamics and stability of protein-ligand interactions. Parameters such as Root Mean Square Deviation (RMSD), Root Mean Square Fluctuation (RMSF), Radius of Gyration (Rg), solvent-accessible surface area (SASA), and intra- and inter-hydrogen bonds were analyzed. RMSD values indicated that all systems reached equilibrium within 10 ns and remained stable, with average RMSD values of 0.26 ± 0.03 nm (APO), 0.36 ± 0.04 nm (ASD), and 0.33 ± 0.05 nm (DRG). RMSF analysis showed average values of 0.13 ± 0.06 nm (APO), 0.14 ± 0.07 nm (ASD), and 0.14 ± 0.06 nm (DRG), indicating that ligand binding did not significantly alter the protein's structural flexibility. Rg values were similar across the APO, ASD, and DRG complexes, suggesting comparable compactness. SASA values (217.44 ± 4.3 nm^2 for APO, 212.49 ± 6.7 nm^2 for ASD, and 218.69 ± 4.3 nm^2 for DRG) demonstrated consistent solvent exposure. Hydrogen bond analysis revealed higher average intra-hydrogen bonds for ASD (356.92 ± 9.92) and DRG (358.88 ± 9.5) compared to APO (351.85 ± 9.1), indicating enhanced stability. The MM-PBSA method showed that ASD and DRG had strong binding affinities, with DRG exhibiting higher van der Wals and electrostatic interactions, while ASD had a more favorable overall binding energy. These comprehensive analyses suggested that the DRG compound forms a more stable and specific interaction with the target protein, supporting its potential as a therapeutic agent.

CONCLUSION

In this study, a flavonoid compound was isolated from the leaf extracts of *E. serratus*. The compound was characterized by its distinct spectroscopic properties and was identified as 3,8-dihydroxy-6-(hydroxymethyl)-2-(3-methoxy-5-methylphenyl)-4H-chromen-4-one, a flavonoid with specific IUPAC names. Through *in-silico* docking studies, it was discovered that the isolated compound (DRG) displayed a higher binding affinity for the target protein than the standard inhibitor (STD). Through molecular dynamics simulations, additional insights were gained into the stability and interactions

within the protein-ligand complex, highlighting the potential of the compound as a therapeutic agent. This study illustrates the potential of flavonoids from *E. serratus* to fight cancer, opening up possibilities for further research in drug development and cancer therapy.

CONFLICT OF INTEREST

The authors declare no conflict of interest

REFERENCES

1. Baruah PS, Deka K, Lahkar L, Sarma B, Borthakur SK, Tanti B. Habitat distribution modelling and reinforcement of *Elaeocarpus serratus* L. - A threatened tree species of Assam, India for improvement of its conservation status. Acta Ecol Sin 2019;39(1):42–9.
2. Raji R, Siril EA. Genetic diversity analysis of promising Ceylon olive (*Elaeocarpus serratus* L.) genotypes using morphological traits and ISSR markers. Curr Plant Biol 2021;26:100201.
3. Tsui C-Y, Yang C-Y. Evaluation of semi-solid-state fermentation of *Elaeocarpus serratus* L. leaves and black soymilk by Lactobacillus plantarum on bioactive compounds and antioxidant capacity. Foods 2021;10(4):704.
4. Geetha DH, Rajeswari M, Jayashree I. Chemical profiling of *Elaeocarpus serratus* L. by GC-MS. Asian Pac J Trop Biomed 2013;3(12):985–7.
5. Freitas De Lima F, Alves Breda C, Lima Cardoso CA, Cristina M, Duarte T, Janet Sanjinez-Argandoña E. Evaluation of nutritional composition, bioactive compounds and antimicrobial activity of *Elaeocarpus serratus* fruit extract. Afr J Food Sci 2019;13(1):30–7.
6. Jayashree I, Geetha DH, Rajeswari M. Evaluation of antimicrobial potential of *Elaeocarpus serratus* L. IJPSR 2014;5(8):3467-72.
7. Das P, Kar P, Hasnu S, Nath S, Tanti B, Hasnu S, et al. Phytochemical screening and antioxidant activity of *Elaeocarpus serratus* L. of Assam. JPP 2017;6(4):866-9.

8. Chen Y-H, Yang C-Y. Ultrasound-assisted extraction of bioactive compounds and antioxidant capacity for the valorization of *Elaeocarpus serratus* L. leaves. Processes 2020;8(10):1218.
9. Parvin MN, Sarwar S, Chowdhury SA, Zakaria HM, Huda NH. In-vitro Cytotoxicity and Antioxidant Studies of *Elaeocarpus serratus*. Stamford J Pharm Sci 1970;2(2):86–90.
10. Huang C-Y, Liu I-H, Huang X-Z, Chen H-J, Chang S-T, Chang M-L, et al. Antimelanogenesis effects of leaf extract and phytochemicals from Ceylon Olive (*Elaeocarpus serratus*) in zebrafish model. Pharmaceutics 2021;13(7):1059.
11. Pinkey AAH, Khan ZI, Taher MA, Soma MA. *Elaeocarpus serratus* L. exhibits potential analgesic and antidiarrheal in mice model. Int J Med Med Res 2020;6(2):44-51.
12. Geetha DH, Jayashree I, Rajeswari M. In vitro antiarthritic activity of *Elaeocarpus serratus* Linn. (Elaeocarpaceae). Int J Pharm Sci Res (IJPSR) 2015;6(6):6264-9.
13. Geetha DH, Jayashree I, Rajeswari M. In Vivo Anti-arthritic activity of Ethanolic Extracts of *Elaeocarpus serratus* L. Int J Pharm Sci Rev Res 2018;48(2):92-7.
14. Geetha DH, Jayashree I, Rajeswari M. Anti-diabetic activity of ethanolic extract of *Elaeocarpus serratus* L. in streptozotocin-induced diabetic rats. Int J Pharm Sci Drug Res 2016;8(01):37–42.
15. Zhang J, Wu Y, Li Y, Li S, Liu J, Yang X, Xia G, Wang G. Natural products and derivatives for breast cancer treatment: From drug discovery to molecular mechanism. Phytomedicine 2024;129:155600. https://doi.org/10.1016/j.phymed.2024.155600.
16. Cragg GM, Pezzuto JM. Natural Products as a Vital Source for the Discovery of Cancer Chemotherapeutic and Chemopreventive Agents. Med Princ Pract 2016;25(Suppl. 2):41–59. https://doi.org/10.1159/000443404.
17. Dokuparthi SK, Reddy TRM. Antioxidant and Nephroprotective Activity of Flavonoid Rich Fraction of *Alphonsea sclerocarpa* Thw. Int J Pharm Sci Drug Res 2021;13(4):384-94.

18. Faseela VA, Maheshwari P. Antioxidant and anticancer activity in leaf extracts of *Elaeocarpus serratus* (L.). Ann. Phytomed., 2024;13(1):1-8. http://dx.doi.org/10.54085/ap.2024.13.1.30
19. Dokuparthi SK, Banerjee N, Kumar A, Singamaneni V, Giri AK, Mukhopadhyay S. Phytochemical investigation and evaluation of antimutagenic activity of the extract of *Cuscuta reflexa* Roxb. by Ames test. Int J Pharm Sci Res 2014;5(8):3430-4.
20. Singamaneni V, Dokuparthi SK, Banerjee N, Kumar A, Chakrabarti T. Phytochemical Investigation and Antimutagenic Potential of Ethanolic Extracts of *Emblica officinalis, Terminalia chebula* and *Terminalia bellirica*. NPJ 2020;10(4):488–94.
21. Fatima M, Edupuganti S. Comparative docking analysis of the phytochemicals isolated from *Landoltia punctata* (G. Mey.) Les & D.J. Crawford. Eur Chem Bull 2023;12(10):5420-34.
22. Sanagala VM, Porika R, Edupuganti S, Dokuparthi SK, Biman KK. Molecular Docking Evaluation of Phytochemicals in Fruits of *Terminalia pallida* Brandis: Implication on Immunomodulation. Trop J Nat Prod Res 2024;8(5):7106-13. https://doi.org/10.26538/tjnpr/v8i5.9.
23. Madej T, Lanczycki CJ, Zhang D, Thiessen PA, Geer RC, Marchler-Bauer A, Bryant SH. MMDB and VAST+: tracking structural similarities between macromolecular complexes. Nucleic Acids Res 2014;42(Database issue).
24. Fatriansyah JF, Boanerges AG, Kurnianto SR, Pradana AF, Fadilah, Surip SN. Molecular Dynamics Simulation of Ligands from *Anredera cordifolia* (Binahong) to the Main Protease (Mpro) of SARS-CoV-2. J Trop Med 2022;2022:1178228. https://doi.org/ 10.1155/2022/1178228.
25. Salo-Ahen OMH, Alanko I, Bhadane R, Bonvin AMJJ, Honorato RV, Hossain S, *et al*. Molecular Dynamics Simulations in Drug Discovery and Pharmaceutical Development. Processes 2021;9(1):71. https://doi.org/10.3390/pr9010071.

Table 1. Docking scores and interactions with proteins.

Ligand	Docking score	Interaction
Isolated Compound	-8.4	CYS437, VAL370, VAL373
Androstenedione (STD)	-7.6	MET364, MET447, PHE430, SER314, PRO429, VAL370, VAL373, CYS437

Table 2. MM – PBSA Analysis results

System	van der Waal energy	Electrostatic energy	Polar solvation energy	Binding energy
ASD	-171.255 ± 13.234 kJ/mol	-13.363 ± 4.969 kJ/mol	88.872 ± 4.155 kJ/mol	-112.925 ± 10.849 kJ/mol
DRG	-186.716 ± 10.310 kJ/mol	-46.321 ± 10.450 kJ/mol	154.372 ± 10.519 kJ/mol	-98.144 ± 12.154 kJ/mol

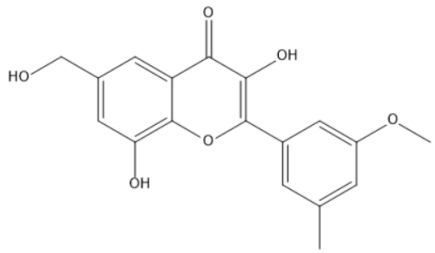

Figure 1. Structure of isolated compound

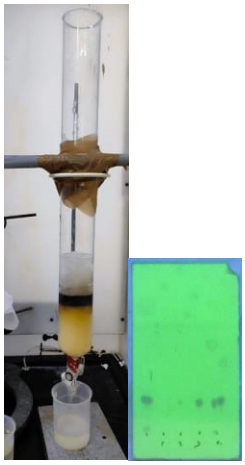

Figure 2. Column chromatography and TLC chromatography

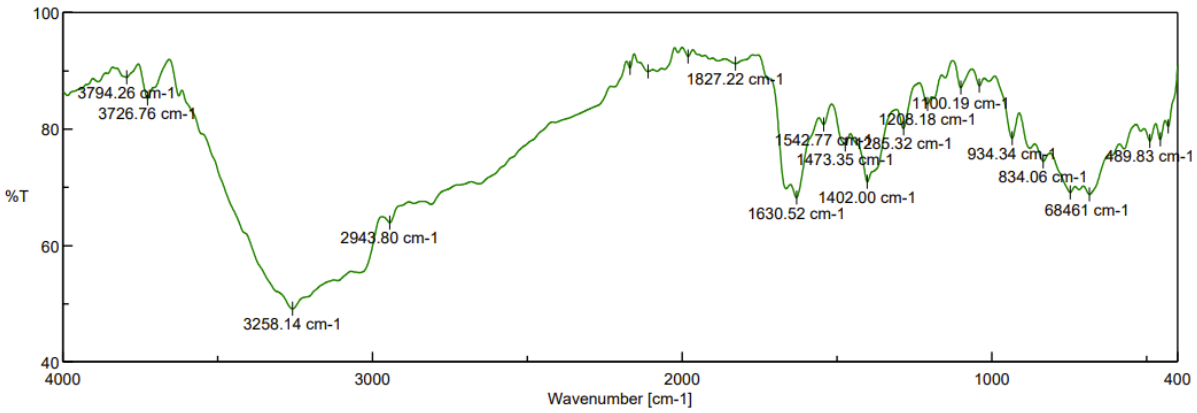

Figure 3. IR spectra

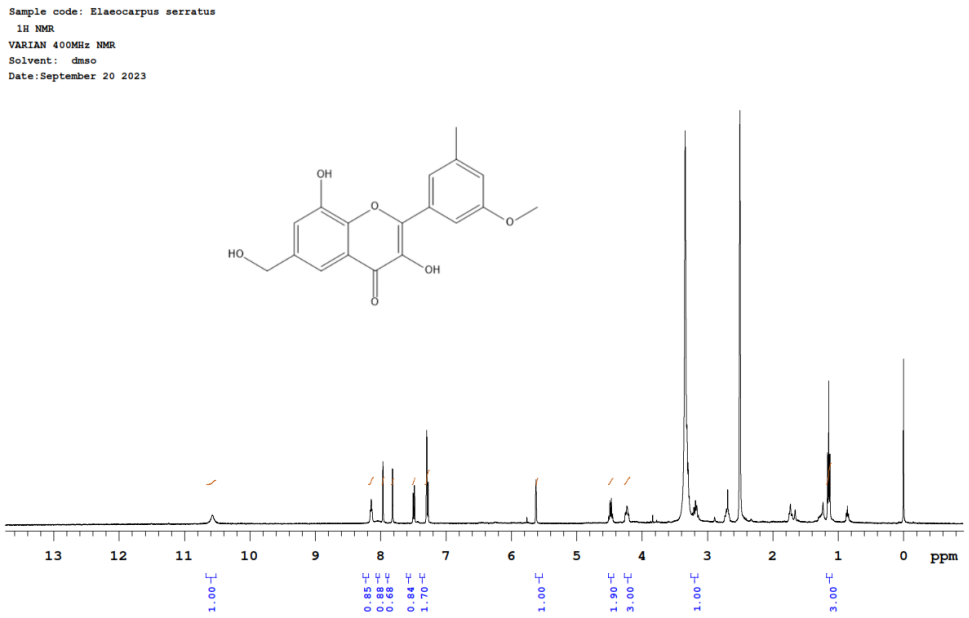

Figure 4. ^{1}H NMR spectra

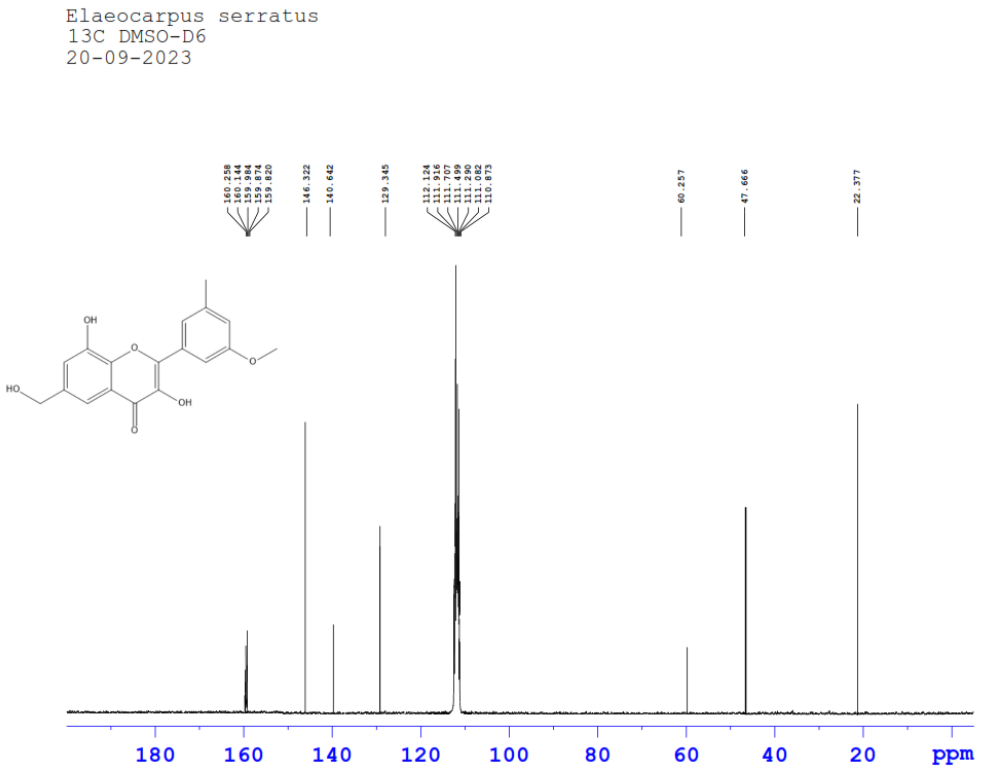

Figure 5. ^{13}C NMR spectra

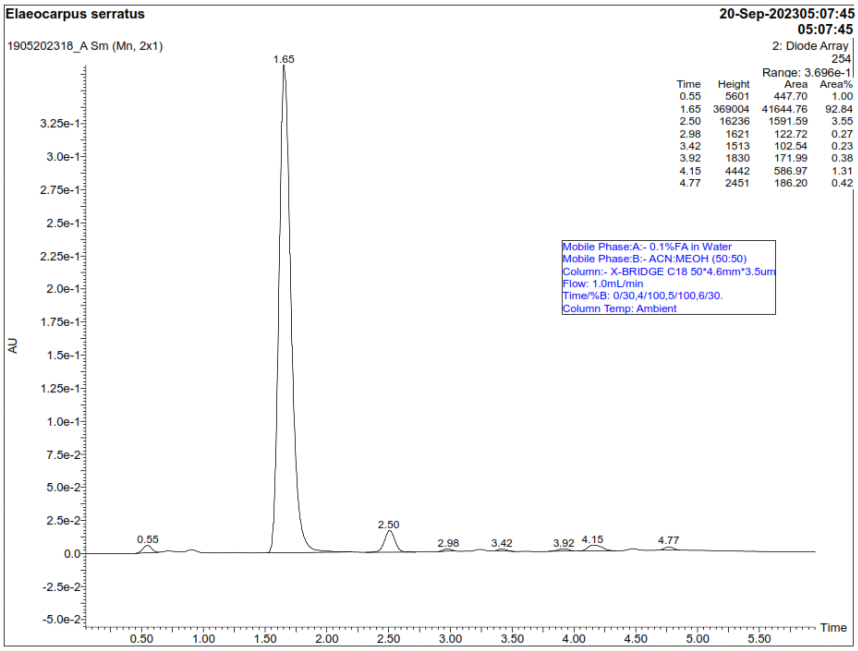

Figure 6. LCMS Chromatogram of the isolated compound

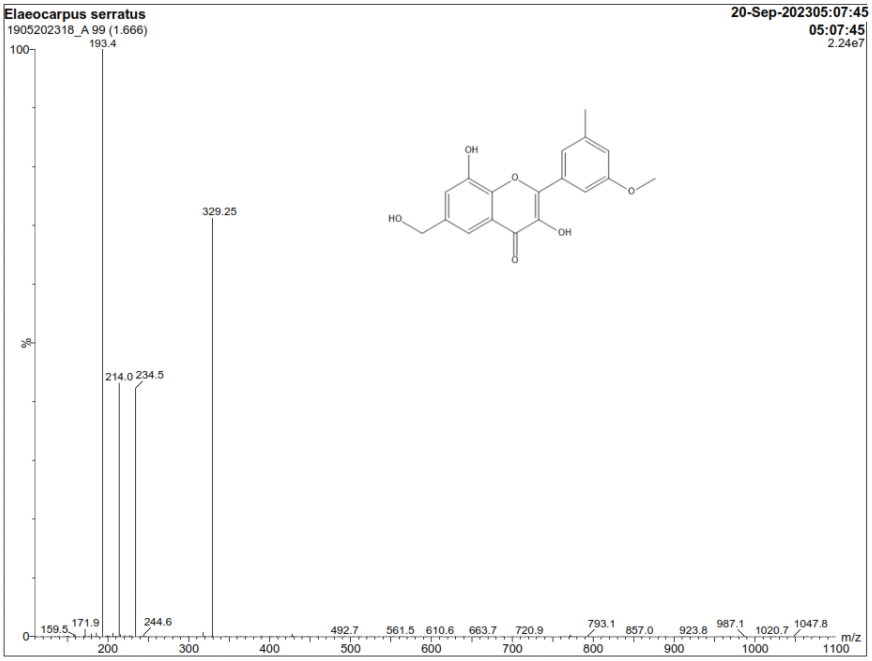

Figure 7. Mass fragmentation pattern of isolated compound

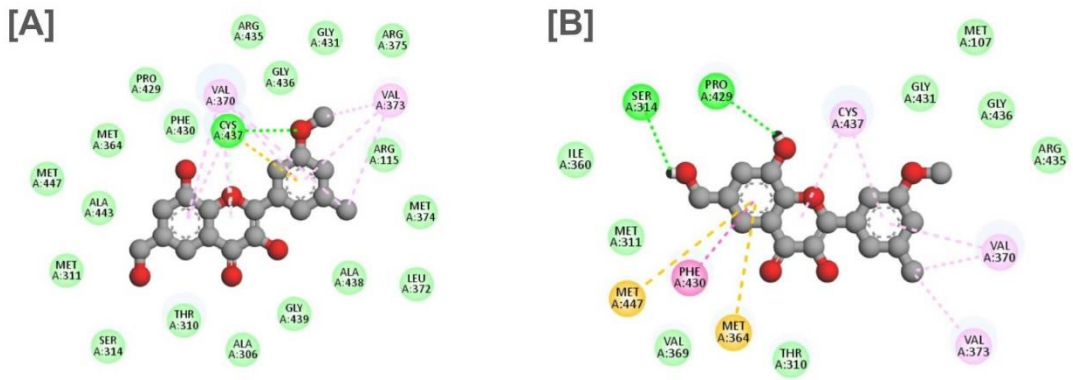

Figure 8. Ligand-Protein interactions

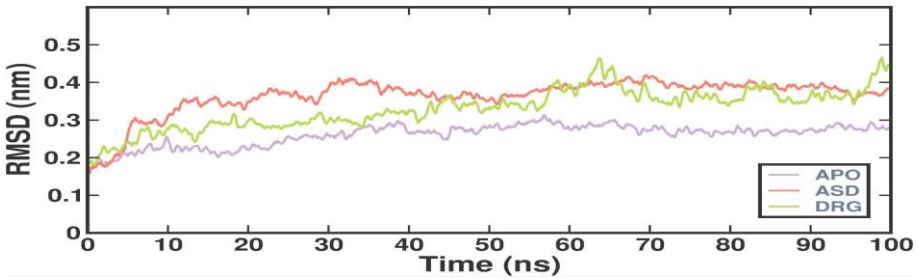

Figure 9. RMSD Conformational dynamics analysis of APO, ASD and DRG

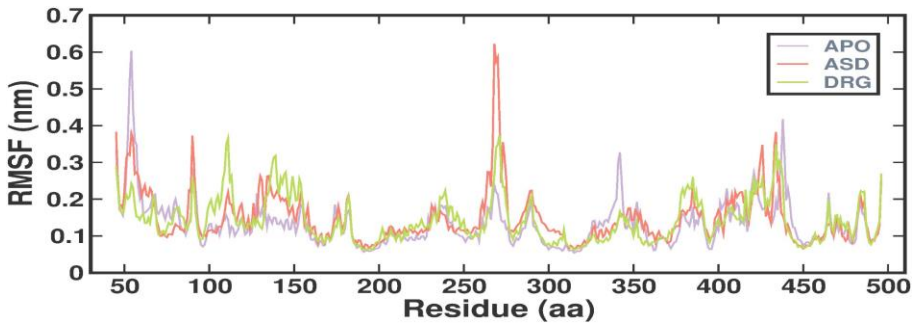

Figure 10. RMSF Conformational dynamics analysis of the APO, ASD, and DRG complexes.

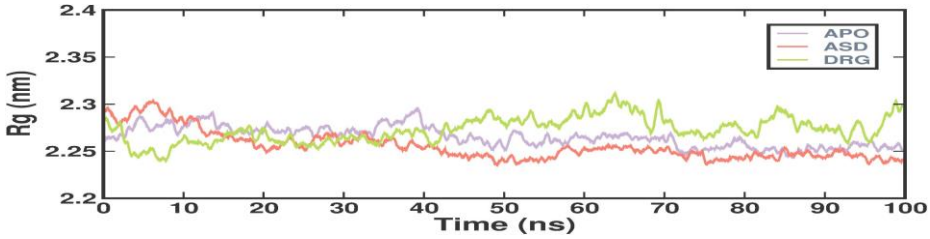

Figure 11. Rg Conformational dynamics analysis of the APO, ASD, and DRG complexes.

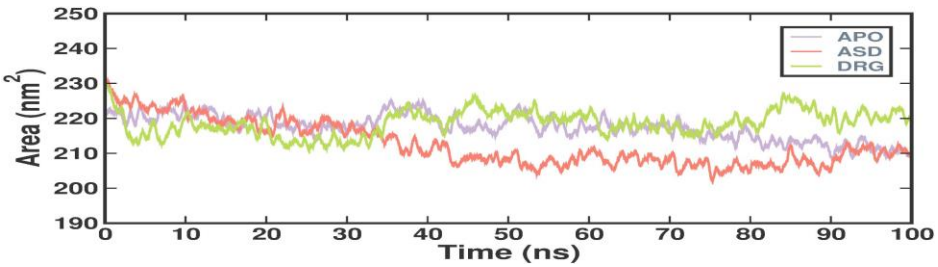

Figure 12. SASA Conformational dynamics analysis of the APO, ASD, and DRG complexes.

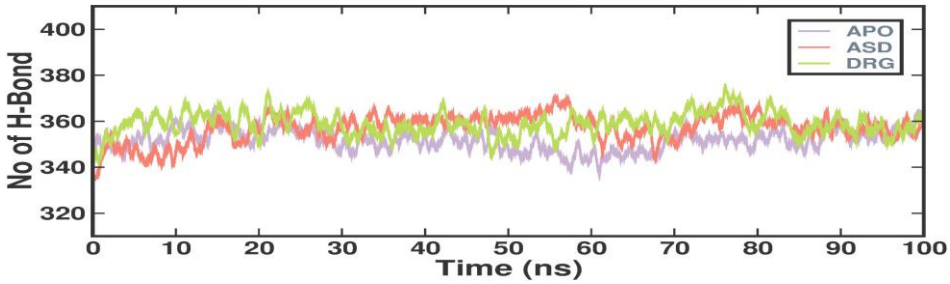

Figure 13. APO, ASD, and DRG intramolecular hydrogen bonds during simulation

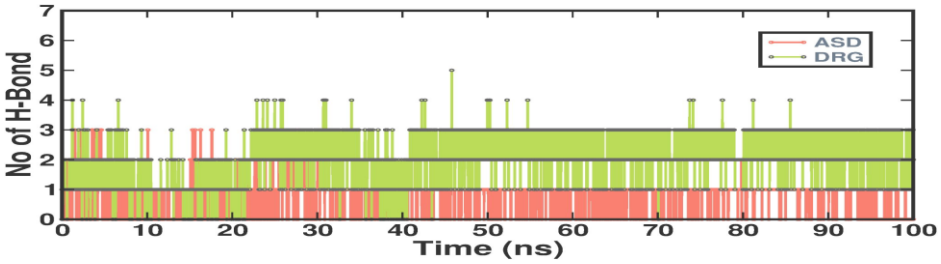

Figure 14. Intermolecular hydrogen bonds between protein ligands during simulation